Three-dimensional coherent structures in a swirling jet undergoing vortex breakdown: stability analysis and empirical mode construction

K. OBERLEITHNER[1]†, M. SIEBER[1], C. N. NAYERI[1], C. O. PASCHEREIT[1], C. PETZ[2], H.-C. HEGE,[2] B. R. NOACK[3] AND I. WYGNANSKI[4]

[1]Hermann-Föttinger-Institut, Technische Universität Berlin, Müller-Breslau Str. 8, D-10623 Berlin, Germany

[2]Abteilung Visualisierung und Datenanalyse, Bereich Numerische Mathematik, Zuse-Institut Berlin, Takustr. 7, D-14195 Berlin-Dahlem, Germany

[3]Département Fluides, Thermique, Combustion, CEAT, Institut Pprime, CNRS – Université de Poitiers – ENSMA, UPR 3346, 43 rue de l'Aérodrome, F-86036 POITIERS CEDEX, France

[4]Department of Aerospace and Mechanical Engineering, The University of Arizona, Tucson, AZ 85721, USA

The spatio-temporal evolution of a turbulent swirling jet undergoing vortex breakdown has been investigated. Experiments suggest the existence of a self-excited global mode having a single dominant frequency. This oscillatory mode is shown to be absolutely unstable and leads to a rotating counter-winding helical structure that is located at the periphery of the recirculation zone. The resulting time-periodic 3D velocity field is predicted theoretically as being the most unstable mode determined by parabolized stability analysis employing the mean flow data from experiments. The 3D oscillatory flow is constructed from uncorrelated 2D snapshots of particle image velocimetry data, using proper orthogonal decomposition, a phase-averaging technique and an azimuthal symmetry associated with helical structures. Stability-derived modes and empirically derived modes correspond remarkably well, yielding prototypical coherent structures that dominate the investigated flow region. The proposed method of constructing 3D time-periodic velocity fields from uncorrelated 2D data is applicable to a large class of turbulent shear flows.

Key words: absolute/convective instability, shear layers, vortex breakdown

1. Introduction

Free and confined strongly swirling jets are of great interest due to their unique feature, commonly known as vortex breakdown. This phenomenon occurs when the ratio of the azimuthal to axial momentum exceeds a certain threshold, while both quantities have to be of the same order of magnitude. Breakdown in swirling jets is characterized by a transition of a jet-like axial velocity profile to a wake-like profile

† Email address for correspondence: kilian.oberleithner@pi.tu-berlin.de

with a local minimum on the axis. This leads to a stagnation point to be followed by a highly turbulent region of reverse flow farther downstream. It can play a crucial role – from desired to detrimental – in a variety of technical applications. For example, vortex breakdown stabilizes the flame of a gas turbine combustor and enhances mixing, thus leading to a reduction of NO_x emissions. On the other hand, bursting of leading-edge vortices adversely affects the lift distribution on delta wings resulting in poor flight performance. Understanding the cause of the vortex breakdown is therefore of great importance in order to develop appropriate control strategies. Furthermore, the transition of the flow from jet-like to wake-like that generates coexisting inner and outer shear layers and the concomitant axial and azimuthal shear makes this flow complex and highly three-dimensional and thus poses a formidable challenge to fundamental studies.

In the present work, we investigate coherent structures of a strongly swirling jet undergoing vortex breakdown. This study is based on experiments carried out at the TU Berlin. 3D time-periodic coherent structures are predicted by stability theory and are constructed from 2D particle image velocimetry (PIV) data via a proposed identification method. In the introductory section we describe the main observed phenomena (§ 1.1), highlight the triple decomposition as the corner stone of our theoretical and experimental study of coherent structures (§ 1.2) and review current definitions of coherent structures in conjunction with stability analyses (§§ 1.3 and 1.4, respectively). Finally, an outline of the paper is provided (§ 1.5).

1.1. *Vortex breakdown studies*

Several types of vortex breakdown have experimentally been observed. Lambourne & Bryer (1962) were the first to describe the axisymmetric and spiral type of vortex breakdown. Swirling jet experiments in pipes conducted by Sarpkaya (1971) and Faler & Leibovich (1978) identified three different types of vortex breakdown, namely the single helical, double helical and bubble-shaped vortex breakdown. Billant, Chomaz & Huerre (1998), investigating a swirling jet at a low Reynolds number, observed an additional conical-shaped breakdown type.

Many researchers found helical disturbances that characterize strongly swirled jets, but their role in the dynamics of vortex breakdown is still a controversial issue. Some experts relate the onset of vortex breakdown to the hydrodynamic instability of vortical flow. Ludwieg (1961) assumes that the formation of a stagnation point results from the sensitivity of the vortex core to helical disturbances. Other researchers describe vortex breakdown as a transition of the flow from a supercritical to a subcritical state similar to a shock wave or a hydraulic jump. According to Escudier & Keller (1985) there is a clear separation of the roles of flow criticality and flow stability. It was proposed that the criticality of the flow determines the basic, wake-like character of the flow and that instability waves are a superimposed fine detail. Recent quantitative investigations could significantly contribute to the understanding of the dynamics accompanying the onset of vortex breakdown. Time-resolved measurements conducted by Liang & Maxworthy (2005) indicate that a recirculation bubble with nearly axisymmetric shape accompanies the first appearance of a stagnation point. It was further noticed that in the wake of this dividing streamline a single helical vortex arises near the jet centre that amplifies until it imposes its frequency onto the entire near field. The authors suggest this to be a self-excited/globally unstable mode, supposably arising from a region of local absolute instability in the lee (downstream) of vortex breakdown. Forced experiments using vortex generators mounted on a rotating nozzle supported the absolute/convective

nature of the dominating instabilities. Gallaire *et al.* (2006) performed a linear stability analysis based on numerical simulations of a swirling jet at $Re = 200$ that were conducted by Ruith *et al.* (2003). They found a convective to absolute instability transition in the lee of the recirculation bubble with a single helical mode being most unstable. Thus, it is likely that the precession of the vortex core and the appearance of strong oscillations that have been observed in experiments and simulations (Ruith *et al.* 2003; Liang & Maxworthy 2005; Duwig & Fuchs 2007; Martinelli, Olivani & Coghe 2007) can be attributed to a self-excited global mode initiated by flow instabilities in the region of vortex breakdown.

1.2. *Triple decomposition as a basis for structure extraction and prediction*

Large-scale organized structures in turbulent flows were investigated for more than 40 years. For a comprehensive summary of earlier work, the reader is referred to Laufer (1975), Roshko (1977), Cantwell (1981) and Ho & Huerre (1984). A variety of definitions and techniques have been developed to reveal these so-called coherent structures. These include statistical approaches, pattern recognition methods, stability theory, conditional sampling and averaging and topological methods from dynamical system theory. Some of these methods are based on a triple decomposition introduced by Hussain & Reynolds (1970). Accordingly, turbulent flow may be decomposed into three constituents: mean (time- or ensemble-averaged), coherent (phase-averaged) and random (incoherent turbulent) motion. The triple decomposition method represents a refinement of the classical Reynolds decomposition. It has become a conventional tool in active flow control (AFC) experiments that distil coherent disturbances by means of phase-locked averaging. Its application to experiments is easy when the coherent structure is tagged by external excitation where a simple synchronization of the data acquisition with the forcing signals is required. Without such external phase trigger, proper orthogonal decomposition (POD)-based techniques can provide another means for phase identification (Depardon *et al.* 2007).

The triple decomposition method has been implicitly used in a number of theoretical articles where the stability analysis was applied for turbulent flows (see, e.g. Crighton & Gaster 1976; Gaster, Kit & Wygnanski 1985). Liu (1989) has developed a local turbulence model for many shear flows utilizing the triple decomposition.

1.3. *Empirical identification of coherent structures*

Large-scale coherent structures in many turbulent shear flows (see, e.g. Van Dyke 1975) are visually similar to predominant instability modes persisting over a wide range of Reynolds numbers. This similarity applies to flows whose mean velocity profiles are inviscidly unstable and whose shape of these profiles does not materially change during the transition from laminar to turbulent flow. This observation suggests that stability considerations can be applied to the mean turbulent flow field, although there is no theoretical basis for this step. However, weakly nonlinear stability approaches explicitly assume that instability modes and most energetic (POD) modes are the same, at least near the onset of a supercritical Hopf bifurcation (Stuart 1958; Noack *et al.* 2003).

Stability theory approximates the flow as a given mean flow and a superposition of space- and time-dependent modes. In similar spirit, turbulent coherent structures can be conceptualized as an expansion of modes. A corresponding least-order representation of a flow snapshot ensemble is obtained by the POD. This approach minimizes a time-averaged residual of the POD expansion for a given number of modes, and it is equipped with further useful analytical properties (Lumley 1967; Holmes, Lumley & Berkooz 1998). Historically, Lumley (1967) introduced POD as a

least-biased definition of coherent structures following up on the analytical approach by Townsend (1956) and the well-known Karhunen–Loéve decomposition from the 1940s.

Meanwhile, many other empirical expansions of flow snapshots have been proposed serving dynamical systems or control theory goals. For instance, the dynamic mode decomposition (DMD) extracts modes from snapshots that are more related to stability eigenmodes (Rowley *et al.* 2009; Schmid 2010). Furthermore, the balanced POD serves as economic expansion for linear input–output relationships (Rowley 2005). The present study is restricted to the classical POD since it targets an optimal kinematical representation of the flow.

1.4. *Linear stability analysis of swirling jets*

Linear stability analysis is presently used to describe the large-scale oscillations observed in this experiment. In principle, self-excited oscillations are known to arise from a region of absolutely unstable flow. They can be described by an unstable global mode (Chomaz 2005) or by local spatio-temporal stability analysis with complex frequency and wavenumber (Huerre & Monkewitz 1990; Monkewitz, Huerre & Chomaz 1993; Pier & Huerre 2001). However, for the underlying flow configuration, we employ a simple local spatial stability analysis to approximate the velocity of the global mode. This simplification serves the main purpose of this study, which is to enhance the understanding of turbulent coherent structures in highly turbulent swirling flows. It is in line with similar studies summarized by Liu (1989), and it is rooted by experimental observations (Oberleithner *et al.* 2009). Strong oscillations at the global frequency were found upstream of vortex breakdown, revealing a precessing vortex core that acts as the global wavemaker. In the outer shear layer, downstream travelling instabilities were detected that were internally forced by the wavemaker and were synchronized to its frequency. These waves served as amplifiers to external forcing, which suggests that the signalling problem is valid for the outer flow region. Assuming that the outer shear layer responds to internal forcing in the same way as to external forcing, we may approximate the large-scale fluctuations downstream of the wavemaker by convectively unstable modes that oscillate at the global frequency. Hence, the spatial analysis presented here was conducted with an unknown complex streamwise wavenumber and the known real global frequency.

Computing spatially growing disturbances in shear layers by means of linear stability analysis has a long history. Michalke (1965) calculated the spatial stability characteristics for the hyperbolic-tangent velocity profile according to inviscid theory. Spatial growth rate and amplitude distribution agreed well with measurements conducted by Freymuth (1966), but they disagreed in some detail when the flow was divergent. As refinement, several attempts have been made to account for non-parallel effects (Gaster 1974; Crighton & Gaster 1976; Plaschko 1979; Gaster *et al.* 1985; Cohen, Marasli & Levinski 1994). Gaster *et al.* (1985) applied the inviscid linear stability analysis to the periodically forced turbulent and slightly divergent mixing layer. The computed normalized phase and velocity amplitudes agreed with experimental data but the amplification rates in the direction of streaming were strongly overpredicted. The robustness of the stability analysis was demonstrated by Weisbrot & Wygnanski (1988), whose computed eigenmodes correctly predicted the measured phase and amplitude distributions of the excited waves, although the latter were forced at high amplitudes clearly exceeding the linear regime. It is important to note that for high Reynolds numbers, the stability analysis is based on the time-averaged turbulent flow which is not a stationary solution of the Navier–Stokes

equation. It is argued that this infringement of the linear stability theory is possible 'knowing that the random changes in the mean velocity occur on a time scale that is short in comparison with the period associated with the large coherent structures' (Weisbrot & Wygnanski 1988).

1.5. *Overview*

The outline of the paper is as follows. The experimental set-up and procedures are described in §2, while the main features that characterize the strongly swirling jet undergoing vortex breakdown are summarized in §3. This flow is dominated by strong oscillations resulting from a self-excited global mode. Two methods to extract the coherent velocity of this mode are introduced in §4. The first method employs linear stability analysis and the second, empirical approach, is based on the POD. Stability analysis provides spatially amplified eigenmodes that represent the amplitude distribution of the phase-averaged velocity. The empirical feature extraction directly provides the measured phase-averaged velocity field by applying a proposed method. Finally, the results of both methods are compared in §5 and a three-dimensional reconstruction of the global mode is presented. It is based on stability analysis and on PIV data providing a portrait of the dominant coherent structures. The main observations are summarized in §6.

2. Experimental arrangement

2.1. *The swirling jet facility*

A turbulent swirling free jet was generated using an apparatus that resembles the one built by Chigier & Chervinsky (1965). The schematic arrangement of the facility is shown in figure 1. The primary axial stream of air passes through a deep honeycomb prior to entering a swirler through which a secondary air stream is introduced through four tangential slots, each 80 mm long. The flow is then guided through a 600 mm long tube, before entering the contraction forming the nozzle. A perforated plate is mounted in the tube to minimize possible inhomogeneities resulting from the tangential inlets in the swirl chamber. The swirl levels generated by the facility depend on the ratio of mass flows coming through the two inlets: a non-swirling jet is generated when no air enters tangentially through the swirler and the maximum swirl level is attained when the axial inflow is zero. Two frequency-controlled blowers provide the necessary airflow. The volume flux of each blower was monitored and controlled by calibrated orifices. The nozzle diameter is $D = 51$ mm.

Particular attention was paid to the design of the excitation device located at the nozzle lip where the thin shear layer between the jet and the quiescent surrounding fluid is unstable to all azimuthal modes (Cohen & Wygnanski 1987; Gallaire, Rott & Chomaz 2004). Acoustic excitation was applied using an array of eight loudspeakers equally spaced along the azimuth (figure 1). Such an array provides radial fluctuations that trigger the inviscid shear layer instabilities. An acoustic wave-guide from each actuator terminates in a rectangular duct leading to a narrow slot that does not interfere with the jet flow when the speakers are inactive. The loudspeakers are driven by a set of digital-to-analogue converters under program control. The actuators are adjusted to equal amplitudes under no-flow conditions using a microphone located at the centreline in the exit plane of the nozzle. The azimuthal disturbances can be controlled by varying the phase difference between the actuators. With an array of eight actuators the highest azimuthal mode numbers that can be excited are $m = \pm 4$.
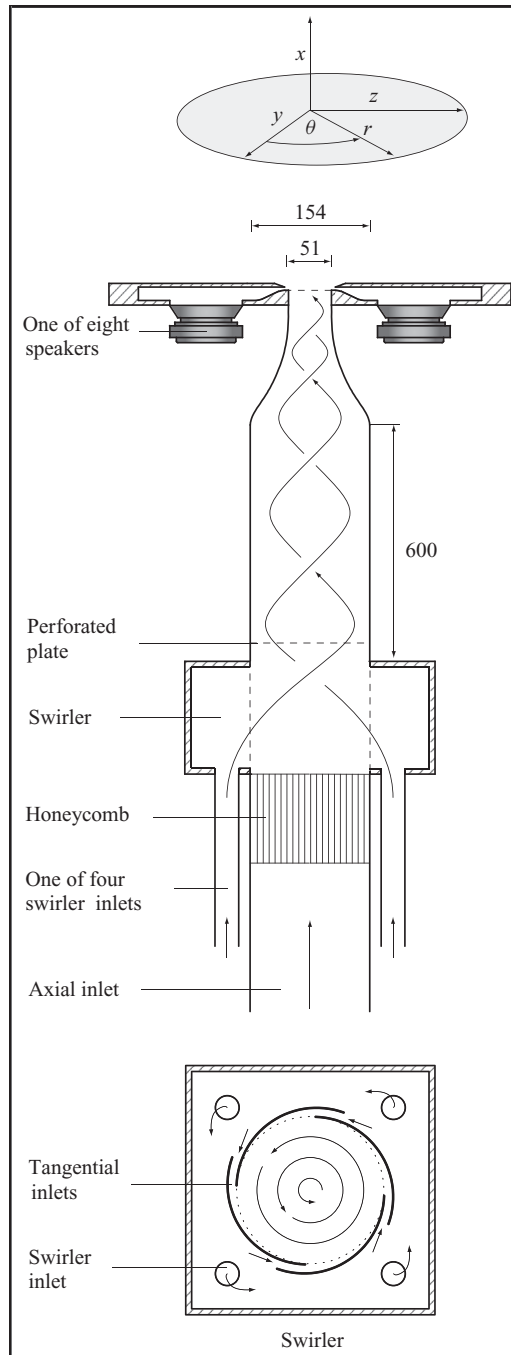
FIGURE 1. Experimental set-up and coordinate systems (all lengths are expressed in mm).

2.2. *Data acquisition*

Stereoscopic particle image velocimetry (Stereo-PIV) was used to measure the flow field. It consists of velocity measurements of particles going through a laser sheet generated by a double-pulsed Nd:Yag laser at 532 nm and 25 mJ in 5 ns burst. Two

CCD cameras with a resolution of 1.3 million pixels were used. Both cameras were positioned at a 45° angle in order to measure all three velocity components in a 2D plane. The cameras and the laser were mounted onto a single traversing system. Data were taken in the crossflow plane as well as in the axial plane. Each ensemble of PIV snapshots consisted of 800 events captured at approximately 3 Hz.

2.3. *Coordinate systems*

The orientation of the two coordinate systems used in the present work is shown in figure 1. Cylindrical coordinates are used to describe the flow quantities in the crossflow plane, whereas Cartesian coordinates are used for data shown in the streamwise plane. The two coordinate systems are necessary, as the latter does not cause a singularity along the jet axis. On the other hand, in the crossflow plane, cylindrical velocity components are necessary to correctly describe the flow quantities of the axisymmetric flow. Furthermore, the normal mode decomposition, necessary for the linear stability analysis, is strictly based on an axisymmetric flow given in cylindrical coordinates. In order to compare theoretical results with experimental data, we will switch between the two coordinate systems.

2.4. *Characteristic numbers*

Two independent dimensionless numbers characterize the global behaviour of the flow:

$$Re_D = \frac{DU}{\nu} \quad \text{with} \quad U = \frac{Q}{\pi(D/2)^2} \tag{2.1}$$

and

$$S = \frac{\dot{G}_\theta}{D/2\dot{G}_x} = \frac{2\pi \int_0^\infty \rho V_x V_\Theta r^2 \, \mathrm{d}r}{D\pi \int_0^\infty \rho \left(V_x^2 - \frac{V_\theta^2}{2} \right) r \, \mathrm{d}r}. \tag{2.2}$$

The Reynolds number Re_D is based on the nozzle diameter D and the average axial velocity U which is derived from the mean mass flow rate Q. The swirl number S is the commonly used parameter that quantifies the amount of swirl (Chigier & Chervinsky 1965; Panda & McLaughlin 1994). It is defined as the ratio between the axial flux of angular momentum $\dot{G}_\theta$ and the axial flux of axial momentum $\dot{G}_x$. According to the conservation of momentum, the swirl number is conserved in the axial direction (Rajaratnam 1976).

3. Flow phenomenology

This paper focuses on the near field of a turbulent jet at a very high rate of swirl. The basic features of this flow are described in the following section in order to explain the motivation for investigating the evolution of the coherent structures.

3.1. *Mean flow properties*

Figure 2 illustrates the streamwise distribution of the time-averaged flow. Due to the occurrence of vortex breakdown, the maximum axial velocity is displaced from the jet centre. The axial velocity profiles have a local velocity minimum in the inner region of the jet. Thus, a wake with a region of reversed flow on and near the jet axis resembles with a recirculation bubble that is bound by upstream and downstream stagnation points. This reversed flow region is similar to the one created by an obstacle placed on the jet centre. Hence, the flow emanating from the nozzle is a swirling ring-jet with an
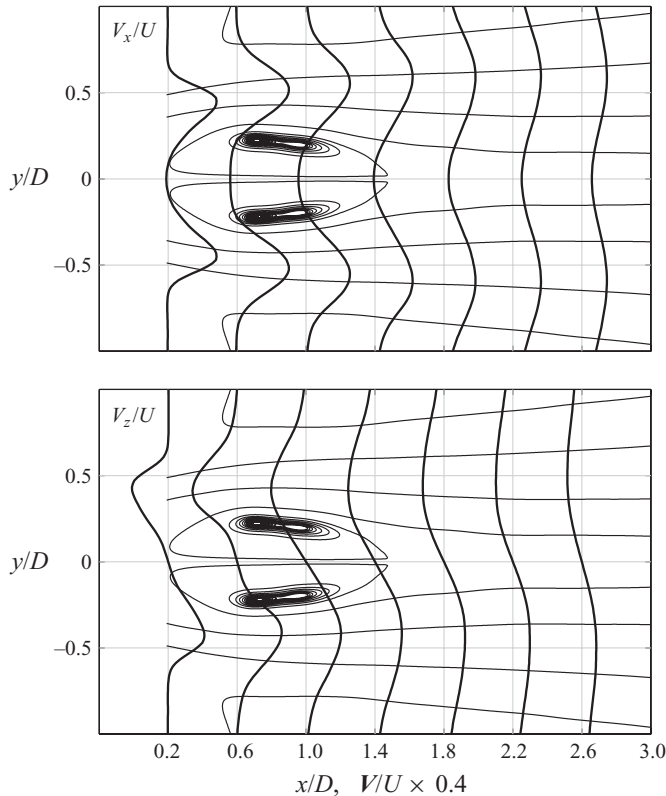
FIGURE 2. Profiles of the time-averaged axial and plane-normal velocity at various axial locations; velocities are normalized by the bulk velocity U; streamlines indicate the location of the recirculation bubble ($Re_D = 20\,000$; $S = 1.22$).

inner and an outer axial and azimuthal shear layer. The streamlines shown in figure 2 illustrate how the flow is guided around the recirculation zone causing a rapid increase of the jet diameter. Downstream the recirculation zone, at approximately $x/D > 1.4$, the inner shear layers begin to merge and the axial velocity on the jet centre increases gradually with increasing downstream distance. The azimuthal velocity profiles may be divided into a vortex core, the region between the jet centre and the maximum azimuthal velocity, and the outer azimuthal shear layer located between the maximum azimuthal velocity and the quiescent surrounding fluid. The axial velocity profile has two inflection points, and thus, in terms of inviscid hydrodynamic stability they possess as many plane instability modes. Since the flow is axisymmetric, these could combine with azimuthal modes. The convex streamlines over the frontal part of the recirculation bubble coupled with the decelerating outer flow provide the necessary conditions for centrifugal instability, as do the concave streamlines in the lee of the bubble coupling with the inner shear layer.

3.2. Self-excited oscillations

Former experimental investigations by Liang & Maxworthy (2005) and numerical simulations of Ruith et al. (2003) revealed that the onset of vortex breakdown is accompanied by energetic large-scale fluctuations. In the present investigation, these strong oscillations had a distinct frequency (figure 3). By traversing a hot-wire probe in
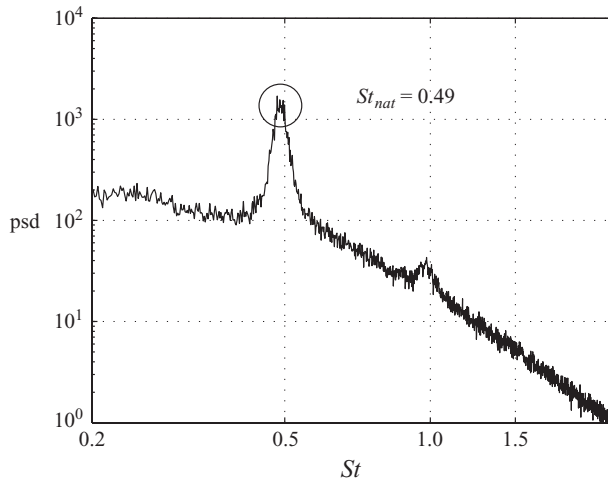
FIGURE 3. Power spectral density of hot-wire-anemometer voltage fluctuations at $(x/D, y/D) = (0.57, 0.38)$ for the unforced swirling jet. The same dominant frequency St_{nat} was measured in the inner and outer axial shear layers. The Strouhal number is defined as $St = fD/U$.

radial and axial directions, a constant dominant frequency was observed throughout the region of interest, with highest amplitudes occurring in the inner and outer axial shear layers. As will be shown later, the spectral peak at $St_{nat} = 0.49$ corresponds to the precession of the vortex core or, in terms of hydrodynamic stability, to the appearance of a strong helical instability with azimuthal wavenumber $m = 1$. This relatively sharp peak is attributed to a self-excited global mode with its origin being located on the jet centreline in the region of reversed flow (Ruith *et al.* 2003; Liang & Maxworthy 2005; Gallaire *et al.* 2006).

There are several experimental techniques to confirm that the flow has transitioned to a global mode via a supercritical Hopf bifurcation. According to Huerre & Monkewitz (1990), near critical conditions, the amplitude of the global mode $|A|$ is governed by the forced Landau equation (Landau & Lifshitz 1959)

$$d|A|/dt = c_1|A| - c_2|A|^3 + f, \tag{3.1}$$

where c_1 is the temporal amplification rate during the time of exponential growth and f is proportional to the external forcing amplitude. In the absence of forcing, the limit cycle amplitude should increase proportionally to the deviation from a control parameter,

$$|A|_{sat} \propto \sqrt{S - S_{crit}}, \tag{3.2}$$

where S_{crit} is the critical control parameter for a constant Reynolds number and $S \geqslant S_{crit}$. The amplitude of the global mode was measured with a calibrated hot wire placed in the centre of the inner axial shear layer at $(x/D, y/D) = (0.57, 0.38)$. At this radial location the oscillations reach their maximum amplitude. A single-wire probe was used with the wire aligned parallel to the azimuthal velocity. The signal was Fourier transformed and the amplitude at the dominant frequency was derived. Figure 4 shows the growth of the global amplitude with increasing swirl while keeping the Reynolds number constant. Evidently, the saturation amplitude is proportional to $\sqrt{S - S_{crit}}$. The linear dependence suggests that the oscillation is of the supercritical Hopf bifurcation type. The critical swirl number was found to be $S_{crit} = 0.88$.
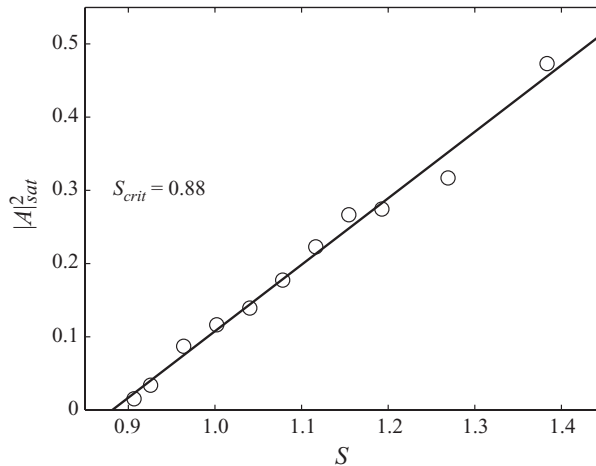
FIGURE 4. The squared saturation amplitude $|A|^2_{sat}$ of the dominant mode as a function of the increasing control parameter S. The open circles represent measurements; the straight line represents a least-squares fit to this data. This linear dependence is characteristic for a supercritical Hopf bifurcation. The zero marks the critical control parameter $S_{crit} = 0.88$. $|A|_{sat}$ is measured with a single hot-wire anemometer placed at $(x/D, y/D) = (0.57, 0.38)$ in the centre of the inner axial shear layer ($Re_D = 20\,000$).

A second experimental technique that may confirm the existence of a self-excited global mode is to investigate the lock-in characteristic. According to Provansal, Mathis & Boyer (1987), Sreenivasan, Raghu & Kyle (1989) and Juniper, Li & Nichols (2009), the critical forcing amplitude at which the frequency of the natural mode St_{nat} locks onto the forcing frequency St_f should linearly depend on $|St_{nat} - St_f|$. The lock-in region is defined as the forcing amplitude at which the spectral peak of the natural mode disappears and the spectrum peaks at the forcing frequency. Measurements conducted with a single hot wire, placed on the centre of the inner axial shear layer at $(x/D, y/D) = (0.57, 0.38)$, revealed that the critical lock-in amplitude is proportional to $|St_{nat} - St_f|$ (figure 5). This provided additional evidence for the existence of a supercritical Hopf bifurcation needed to establish a global mode.

Concluding this section, the base flow under investigation is a swirling ring-jet whose conical boundaries originate at the orifice due to a recirculation zone located on the jet axis. The axial and azimuthal shear layers coexist in the outer region of the jet and in the jet core. The swirl number considered presently is above the critical value at which a supercritical Hopf bifurcation takes place. Thus, the strong coherent fluctuations that are dominating the entire flow field near the nozzle are attributed to the existence of a self-excited global mode.

4. Extraction of coherent structures

Two approaches are outlined in this section in order to extract the coherent structures from overall turbulence. In §4.1, the theoretical considerations and numerical implementation of the linear stability analysis are described. In §4.2, the empirical extraction of coherent structures by means of the POD is introduced. Moreover, it is proposed how to reconstruct the three-dimensional shape of the structure from two-dimensional empirical data. The results of the presented methods are compared in the subsequent section.

	Cartesian	Cylindrical
$\boldsymbol{x}$	(x, y, z)	(x, r, θ)
$\boldsymbol{V}$	(V_x, V_y, V_z)	(V_x, V_r, V_θ)
$\boldsymbol{v}^c$	(v_x^c, v_y^c, v_z^c)	$(v_x^c, v_r^c, v_\theta^c)$
$\boldsymbol{v}^s$	(v_x^s, v_y^s, v_z^s)	$(v_x^s, v_r^s, v_\theta^s)$

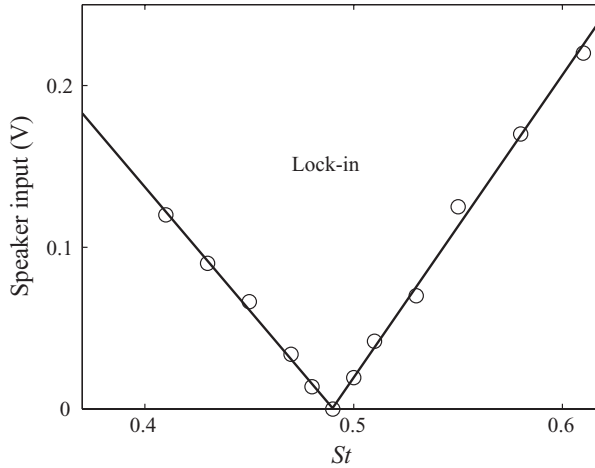TABLE 1. Coordinate system and corresponding velocity components.

FIGURE 5. Critical loudspeaker input voltage at which the global mode locks onto the forcing frequency. The open circles mark measurement values and the the solid lines represent fits to these data. The linear dependence of the threshold amplitude on $|St_{nat} - St_f|$ is another indicator of a supercritical Hopf bifurcation to a global mode. The flow was forced at the orifice at $m = 1$ which is the azimuthal wavenumber of the natural mode. The natural frequency is $St_{nat} = 0.49$ ($Re_D = 20\,000$; $S = 1.22$)

For the following considerations, we decompose all flow variables into three parts (Hussain & Reynolds 1970): steady mean flow, coherent component and stochastic fluctuations:

$$\boldsymbol{v}(\boldsymbol{x}, t) = \boldsymbol{V}(\boldsymbol{x}) + \boldsymbol{v}^c(\boldsymbol{x}, t) + \boldsymbol{v}^s(\boldsymbol{x}, t), \qquad (4.1)$$

with the phase-averaged velocity $\boldsymbol{v}^p = \boldsymbol{V}(\boldsymbol{x}) + \boldsymbol{v}^c(\boldsymbol{x}, t)$. Table 1 summarizes the symbols used to distinguish between the different parts of the velocity components in their corresponding coordinate systems.

4.1. *Theoretical approach based on the linear stability analysis*

We shall assume that the mean flow is known and introduce its analytical approximation followed by an outline of the theoretical considerations and the numerical procedures used in the linear stability analysis.

4.1.1. *Analytic representation of the time-averaged flow*

The incompressible mean flow of the unconfined swirling jet is expressed by an axial velocity V_x and a circumferential velocity V_θ. The radial velocity is neglected. The characteristic velocity scale $V = V_{x,max}$ is defined as the maximum axial velocity at a certain axial location, and the characteristic length scale $R = r_{x,max}$ is represented by the radial distance of the maximum velocity. The 'Monkewitz profile' approximates
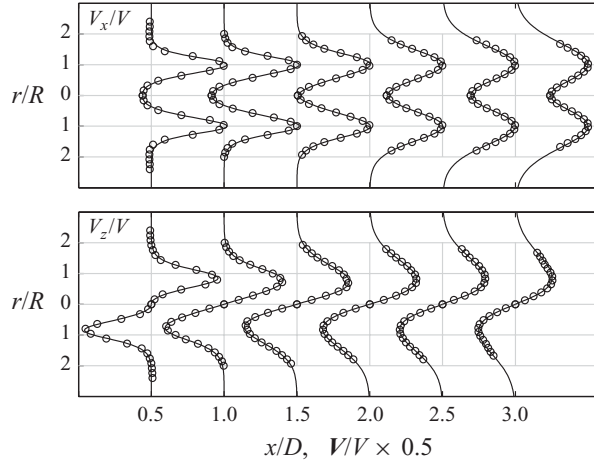
FIGURE 6. Velocity profiles of the approximated mean flow field using the shape parameters listed in table 3. Symbols refer to experimental data.

the axial component if we normalize all velocities by V and all lengths by R. In the current study, we employ a modification of this profile introduced by Michalke (1999):

$$V_x = 4BF_1[1 - BF_2], \qquad (4.2a)$$

where F_1 and F_2 are given by Monkewitz & Sohn (1988) as

$$F_j = \left[1 + \left(\mathrm{e}^{r^2 b_j} - 1\right)^{N_j}\right]^{-1}, \quad j = 1, 2. \qquad (4.2b)$$

The quantity B depends on the axial velocity on the jet centreline V_{cl}:

$$B = 0.5[1 + (1 - V_{cl})^{1/2}]. \qquad (4.2c)$$

$N_{1,2} \geqslant 1$ are the shape parameters that control the thickness of the jet shear layers. In contrast to Michalke (1999), we use two parameters N_1 and N_2 in order to approximate the inner and outer shear layer, respectively. The normalized swirl component is represented by the same equations with the simplification that $B = 1$. Therefore, the local swirl parameter $S_{loc} = V_{\theta,max}/V_{x,max}$ is introduced yielding

$$V_\theta = 4F_3[1 - F_4]S_{loc}. \qquad (4.3)$$

Note that all flow parameters and fitting parameters of (4.2)–(4.3) vary in the axial direction due to the non-parallelism of the mean flow. Their quantities are displayed in tables 2 and 3 for profiles taken at $x/D = [0.25; 0.5; 1; 1.5]$. The fitted velocity profiles are displayed in figure 6 together with the measured mean axial and azimuthal velocities for distances in the range $0.5 \leqslant x/D \leqslant 3$. Both velocity components are well represented by the suggested approximation. Note that this rather complex mean flow approximation is necessary to accurately represent the two axial and azimuthal shear layers. Simpler models as introduced by Michalke (1999) and Gallaire, Chomaz & Huerre (2004) did not approximate the underlying mean flow well enough for an accurate linear stability analysis.

4.1.2. *Eigenvalue problem*

To analyse the linear stability at a given axial location of the mean flow, velocity and pressure disturbances $(v_x^c, v_r^c, v_\theta^c)$ are superposed onto the corresponding mean

x/D	V/U	S_{loc}	R/D	B
0.25	0.87	0.91	0.45	1.01
0.50	0.76	0.90	0.50	1.03
1.00	0.63	0.81	0.56	1.04
1.50	0.51	0.71	0.58	1.00

TABLE 2. Flow parameters of mean flow approximation (4.2)–(4.3).

x/D	N_1	N_2	N_3	N_4	b_1	b_2	b_3	b_4
0.25	4.23	1.10	4.18	0.73	0.51	0.38	0.51	0.27
0.50	3.14	1.35	2.23	1.09	0.56	0.52	0.73	0.66
1.00	2.92	1.06	1.87	0.55	0.53	0.46	0.63	0.35
1.50	2.38	0.87	1.17	0.56	0.46	0.35	0.71	0.57

TABLE 3. Fitting parameters of mean flow approximation (4.2)–(4.3).

velocity profile expressed by (4.2)–(4.3). These perturbations are decomposed in the classical form

$$\left(v_x^c, v_r^c, v_\theta^c, p^c\right) = Re\left\{[H, iF, G, P]\exp[i(\alpha x + m\theta - \omega t)]\right\}, \tag{4.4}$$

where H, F, G and P are the eigenfunctions, $\alpha = \alpha_r + i\alpha_i$ is the complex axial wavenumber, m is the integer azimuthal wavenumber and $\omega = \omega_r + i\omega_i$ is the complex angular frequency. Upon substituting the modal decomposition (4.4) into the Navier–Stokes equations, linearized about the prescribed mean flow (4.2)–(4.3), we obtain the linear system of ordinary differential equations for continuity

$$F' + \frac{F}{r} + \frac{mG}{r} + \alpha H = 0, \tag{4.5a}$$

for the x-momentum

$$\frac{H''}{Re} + \frac{H'}{rRe} + \left[i\omega - \frac{imV_\theta}{r} - i\alpha V_x - m^2 r^2 Re\right]H - iV_x'F - i\alpha P = \frac{\alpha^2 H}{Re}, \tag{4.5b}$$

for the r-momentum

$$\frac{iF''}{Re} + \frac{iF'}{rRe} - \left[\omega - \frac{mV_\theta}{r} - \alpha V_x + \frac{i(m^2 + 1)}{r^2 Re}\right]F - 2\left[\frac{im}{r^2 Re} - \frac{V_\theta}{r}\right]G - P' = \frac{i\alpha^2 F}{Re}, \tag{4.5c}$$

and for the θ-momentum

$$\frac{G''}{Re} + \frac{G'}{rRe} + \left[i\omega - \frac{imV_\theta}{r} - i\alpha V_x - \frac{m^2 + 1}{r^2 Re}\right]G$$
$$- \left[iV_\theta' + \frac{2m}{r^2 Re} + \frac{iV_\theta}{r}\right]F - \frac{imP}{r} = \frac{\alpha^2 G}{Re}, \tag{4.5d}$$

where the primes denote d/dr. For the free jet, the boundary conditions in the far field are

$$F(\infty) = G(\infty) = H(\infty) = P(\infty) = 0 \tag{4.6}$$

and in the limit along the centreline ($r = 0$) impose

$$F(0) = G(0) = H(0) = P(0) = 0 \quad \text{if } |m| > 1 \qquad (4.7a)$$

$$\left. \begin{array}{c} H(0) = P(0) = 0 \\ F(0) + mG(0) = 0 \\ 2F'(0) + mG'(0) = 0 \end{array} \right\} \quad \text{if } |m| = 1 \qquad (4.7b)$$

$$\left. \begin{array}{c} F(0) = G(0) = 0 \\ H(0) \quad \text{and} \quad P(0) \text{ finite} \end{array} \right\} \quad \text{if } m = 0. \qquad (4.7c)$$

For a given mean velocity profile, the system (4.5)–(4.7) describes an eigenvalue problem. A non-zero solution of (F, G, H, P) exists if and only if the complex pair (α, ω) satisfies the dispersion relation $\mathcal{D}(\alpha, \omega, m, \Gamma, Re) = 0$. The symbol Γ represents all control parameters describing the mean velocity profiles.

In the present work, the linear stability analysis is performed to derive the spatial modes that are retrieved by phase-averaged measurements. Thus, the focus is on the viscous spatial stability analysis where the *spatial branches* $\alpha(\omega, \Gamma)$ are obtained by solving for complex axial wavenumbers when ω and m are real. The non-parallelism of the mean flow requires to solve the eigenvalue problem (4.5)–(4.7) at each axial location. The slowly varying amplitudes are expressed by the local eigenmodes. The full solution is then constructed by using the eigenfunctions that depend on x and on the global parameters ω and m and a carrier wave $\exp\left(\int_0^x \alpha(x) \, \mathrm{d}x + m\theta - \omega t\right)$. The Reynolds number in (4.5) is based on the characteristic length and velocity scale $Re = RV/\nu$ and is also varying with x. The flow will be considered as unstable when the disturbance grows with x, i.e. when the imaginary part of the eigenvalue α_i is negative. The existence of saddle points in the complex α plane, which serve as an indicator for absolute instability, will not be investigated.

4.1.3. *Numerical method*

Khorrami, Malik & Ash (1989) demonstrated that the eigenvalue problem can be efficiently solved by using a Chebyshev spectral collocation method. Following this study, the system of ordinary differential equations (4.5) is solved numerically by discretizing the three velocity components and the three momentum equations at the Chebyshev collocation points. The continuity equation is enforced at the mid grid points. This approach has been successively applied by Khorrami (1991) to the temporal problem and recently to the spatial problem by Parras & Fernandez-Feria (2007). For a detailed description of the numerical procedure, the reader is referred to Khorrami *et al.* (1989); thus, only a brief summary is given here.

The boundary conditions (4.6) are enforced at a large but finite radius $r_{max} \gg 1$ as was done by Olendraru & Sellier (2002) and Parras & Fernandez-Feria (2007). A coordinate transformation is necessary to map the Chebyshev collocation points, in the interval $-1 \leqslant \xi \leqslant 1$, onto the physical domain of the problem, in the range $0 \leqslant r \leqslant r_{max}$. Here, the two-parameter transformation proposed by Malik, Zang & Hussaini (1985) is used, which reads

$$\frac{r}{r_c} = \frac{1 + \xi}{1 - \xi + 2r_c/r_{max}}. \qquad (4.8)$$

Since the Chebyshev collocation points are known to be distributed in the vicinity of $r = 0$ and r_{max}, the parameter r_c is necessary to redistribute the collocation points. It allows half of the points to be distributed in the region $0 \leqslant r \leqslant r_c$.

Finally, the eigenvalue problem (4.5) for the case of spatial stability (given real ω, complex eigenvalue α) is linearized by introducing a generalized eigenvector $X = [F, G, H, \alpha F, \alpha G, \alpha H, P]^{\mathrm{T}}$. Discretizing the system of ordinary differential equations (4.5) in terms of the variable ξ and enforcing the boundary conditions (4.6)–(4.7), we may write the generalized eigenvalue problem as

$$\boldsymbol{D}X = \alpha\boldsymbol{E}X. \tag{4.9}$$

Taking Z as the number of Chebyshev points, both $\boldsymbol{D}$ and $\boldsymbol{E}$ are square matrices with dimensions of $7Z$. Note that the last 14 rows of matrix $\boldsymbol{D}$ contain the boundary conditions. The eigenvalue problem (4.9) is solved using a standard EIG routine embedded in the software environment MATLAB$^{\mathrm{TM}}$. Spurious eigenmodes, caused by the discretization, are discarded by two independent criteria: first, all eigenmodes are discarded that do not diminish at $r \to \infty$, that is to say that we consider only those eigenvalues satisfying

$$\frac{\displaystyle\sum_{i=1}^{Z/10} |F(r_i)|^2}{\displaystyle\sum_{i=1}^{Z} |F(r_i)|^2} < \epsilon_1 \tag{4.10}$$

with r_i being the radial points and ϵ_1 a given tolerance. Second, spurious eigenvalues are filtered out by comparing the computed spectra $\mathscr{S}_Z$ and $\mathscr{S}_{Z'}$ for $Z' > Z$. The location of the spurious modes in the complex α-plane is very sensitive to the number of Chebyshev points Z, in contrast to the few physical eigenvalues of the problem. Thus, the eigenvalues α are considered as spurious if $\min|\alpha - \alpha'| > \epsilon_2$.

The accuracy of our calculations is first checked by comparing the computed eigenvalues with those calculated by Khorrami *et al.* (1989) and Parras & Fernandez-Feria (2007). Our computed eigenvalues agree for all shown digits which is not surprising as these authors use exactly the same numerical method. A comparison of our computations with the results presented by Gallaire & Chomaz (2003) is more challenging as their results are retrieved by direct numerical simulations of the linear impulse response. Unfortunately, Gallaire & Chomaz do not explicitly present computed eigenvalues of their spatio-temporal analysis but only display the complex frequency ω of the temporal problem. Hence, for the sake of comparison, we computed the temporal modes using the same base flow as used by Gallaire & Chomaz. Figure 7 clearly shows that for $m = 1$ both numerical methods arrive at the same solutions. The correctness of the computed eigenvalues makes us confident to apply the computations to our base flow. In comparison to the base flow used by Gallaire & Chomaz and Parras & Fernandez-Feria, our mean flow is more complex as it consists of two axial and two azimuthal shear layers. Furthermore, the Reynolds number is in the range of $3000 \leqslant Re \leqslant 8000$, i.e. one order of magnitude higher than that used by Gallaire & Chomaz. Thus, from the numerical point of view the problem is more demanding and the number of collocation points has to be increased. To satisfy the filter criterion (4.10) and to successfully discard the spurious eigenvalues, the number of Chebyshev points is increased to $Z = 300$. A convergence study optimizes the parameters a and r_{max} of the transformation (4.8) yielding $a = 3$ and $r_{max} = 100$ for all computations presented here. It was observed that the calculated eigenvalues are relatively insensitive to the radial distribution of the collocation points.
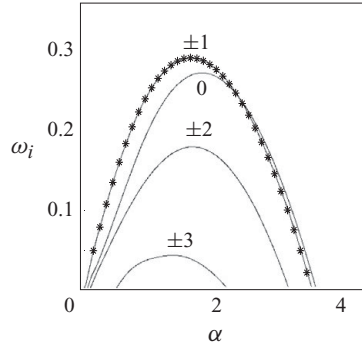
FIGURE 7. Temporal stability analysis of a non-swirling jet. The growth rate ω_i is plotted over the axial wavenumber α. The corresponding azimuthal wavenumbers m are shown close to the corresponding curves. The solid lines represent computations reprinted from Gallaire & Chomaz (2003). Symbols represent our computations at $m \pm 1$ using a Chebyshev collocation method ($Z = 180$, $a = 3$, $r_{max} = 100$, $\epsilon_1 = 10^{-11}$, $\epsilon_2 = 10^{-3}$).

A further challenging aspect of the computation of spatial instability is the sorting of the eigenvalues and eigenfunctions with respect to the corresponding modes. Spatial branches have to be identified and tracked in the complex wavenumber plane while a parameter of the dispersion relation is changed. A well-designed sorting routine is of great importance to accurately follow the spatial branches into the region of negative growth $\alpha_i > 0$. In this region, many modes coexist and several spatial branches intersect. We developed a routine which sorts the eigenvalues and eigenfunctions of the dispersion relations $\mathscr{D}$ and $\mathscr{D}'$ by incorporating two criteria: first, eigenvalues are sorted by minimizing the distance $|\alpha - \alpha'|$; second, the normalized eigenvectors X are sorted by minimizing $|1 - \langle XX' \rangle|$. The efficiency of the sorting routine was validated by visually checking the spatial branches.

4.2. *Empirical approach based on the POD*

In this section, we outline the path from the POD of 2D PIV data to the construction of full 3D time-dependent velocity field.

4.2.1. *Proper orthogonal decomposition*

We consider the fluctuation snapshots of a velocity field

$$v'(x, t_k) = v(x, t_k) - V(x), \tag{4.11}$$

where x is a point in a spatial domain $\Omega \subset \mathbb{R}^3$, and t_k, $k = 1, \ldots, N$, are the sampling instants. The goal is to find a least-order expansion of the snapshots

$$v'(x, t_k) = \sum_{p=1}^{I} a_p(t_k) \boldsymbol{\Phi}_p(x) + v_{res}(x, t_k), \tag{4.12}$$

which minimizes the residual v_{res} in a sense specified below. The snapshots are considered as elements of the Hilbert space of square integrable vector fields $\mathscr{L}_2(\Omega)$. This Hilbert space is equipped with the inner product in Ω between two vector fields v and w defined by

$$(v, w)_\Omega := \int_\Omega v \cdot w \, dx, \tag{4.13}$$

and the related norm $\|\boldsymbol{v}\|_\Omega$ reads

$$\|\boldsymbol{v}\|_\Omega := \sqrt{(\boldsymbol{v}, \boldsymbol{v})_\Omega}. \tag{4.14}$$

The velocity fields are provided by PIV snapshots taken at N uncorrelated points at the times t_k, $k = 1, \ldots, N$. In addition to the inner product in space, we define the ensemble average of a quantity ζ as

$$\overline{\zeta} := \frac{1}{N} \sum_{k=1}^{N} \zeta(t_k). \tag{4.15}$$

The quantity ζ may be a scalar, a vector or any other tensor. The norm and ensemble average allows one to formulate an optimal property of the Galerkin expansion (4.12). We require that the spatial modes are chosen such that the time-averaged $\mathscr{L}_2$ error is minimal for the number of modes $I = 1, \ldots, N$:

$$\chi_2(\boldsymbol{\Phi}_1, \ldots, \boldsymbol{\Phi}_I) := \overline{\|\boldsymbol{v}_{res}\|^2} = \min. \tag{4.16}$$

Note that the minimized residual $\boldsymbol{v}_{res} \equiv 0$ for $I = N$. This optimality property is fulfilled by the snapshot POD modes introduced by Sirovich (1987). The corresponding algorithm is based on the $N \times N$ autocorrelation matrix $\boldsymbol{R} = (R_{kl})$ defined by

$$R_{kl} := \frac{1}{N} (\boldsymbol{v}'(\boldsymbol{x}, t_k), \boldsymbol{v}'(\boldsymbol{x}, t_l))_\Omega \tag{4.17}$$

quantifying the relation between the snapshots. The correlation matrix is symmetric and positive semi-definite, i.e. the eigenvalue problem

$$\boldsymbol{R}\boldsymbol{a}_p = \lambda_p \boldsymbol{a}_p \tag{4.18}$$

has real and non-negative eigenvalues $\lambda_p \geqslant 0$. Without loss of generality, we assume the eigenvalues to be sorted by magnitude:

$$\lambda_1 \geqslant \lambda_2 \geqslant \cdots \geqslant \lambda_N = 0. \tag{4.19}$$

Note that $\lambda_N = 0$ since N linearly independent snapshots cannot span the whole N-dimensional space. Two points, for instance, define a one-dimensional line. The corresponding eigenvectors $\boldsymbol{a}_p := [a_p(t_1), \ldots, a_p(t_N)]^T$, called temporal modes, are orthogonal by construction. For reasons of convenience, we require

$$\overline{a_p a_q} = \frac{1}{N} \sum_{k=1}^{N} a_p(t_k) a_q(t_k) = \lambda_p \delta_{pq}. \tag{4.20}$$

Now, the spatial POD modes can be calculated as a linear combination of the fluctuation snapshots

$$\boldsymbol{\Phi}_p(\boldsymbol{x}) = \frac{1}{N\lambda_p} \sum_{k=1}^{N} a_p(t_k) \boldsymbol{v}'(\boldsymbol{x}, t_k). \tag{4.21}$$

These spatial POD modes are orthonormal by construction:

$$(\boldsymbol{\Phi}_p, \boldsymbol{\Phi}_q)_\Omega = \delta_{pq}. \tag{4.22}$$

The eigenvalues λ_p represent twice the amount of the fluctuating kinetic energy contained in each POD mode, $K_p := \overline{(\boldsymbol{v}', \boldsymbol{\Phi}_p)_\Omega^2}/2 = \lambda_p/2$. The total fluctuation energy
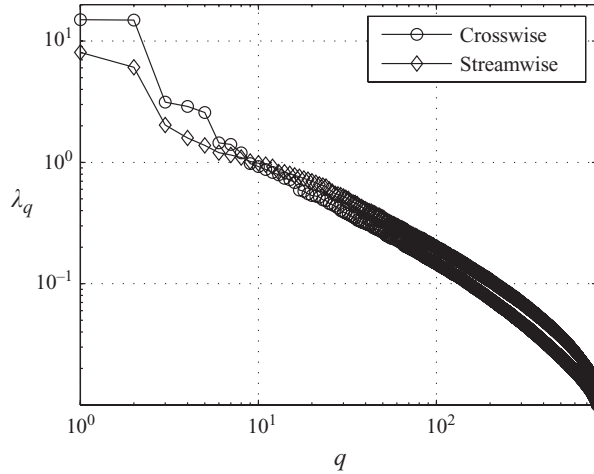
FIGURE 8. POD spectrum of the velocity modes p for the crossflow and streamwise planes of measurement. TKE is expressed in per cent of the sum $K = \sum_{p=1}^{N} K_p$.

is defined as the sum of the modal contributions owing to orthonormality (4.22):

$$K := \frac{1}{2}\overline{\|\boldsymbol{v}'\|_{\Omega}^2} = \sum_{p=1}^{N} K_p = \frac{1}{2}\sum_{p=1}^{N} \lambda_p. \tag{4.23}$$

K is generally referred to as turbulent kinetic energy (TKE). Snapshot POD extracts the most energetic structures representing them as linear combinations of the snapshots and imposes orthogonality in spatial and temporal modes. Snapshot POD is the time-discrete variant of a general continuous formulation (Holmes *et al.* 1998). In turbulent flows, the large-scale structures usually contain a major portion of the TKE, so the POD modes with high energy content can hence be expected to span the basis for the dominant coherent structures.

4.2.2. *Spatial and temporal POD modes*

The snapshot POD, as described above, is applied to the data taken in the crossflow and streamwise planes of measurement. Both sets of measurement consist of 800 snapshots. The observation domains have a spatial extent of $-1.1 < y/D < 1.1$ and $-1.1 < z/D < 1.1$ at $x/D = 0.57$ for the crossflow plane and $0.25 < x/D < 3$ and $-1.1 < y/D < 1.1$ at $z/D = 0$ for the streamwise plane. The eigenvalue spectrum of POD modes for both measurement planes is shown in figure 8.

For both cases the POD shows that the first two eigenvalues contain substantial amount of energy. In the crossflow plane the first two modes contain already 30 % of TKE, while in the streamwise plane these modes contain more than 14 %. In both cases, the energy contained in the two leading modes is nearly equal suggesting that the two modes span a travelling wave.

In the crossflow plane of measurement, the first and second spatial POD modes resemble one another as do the fourth and fifth modes (figure 9). The first pair of modes describes an azimuthal wave represented by two modes having a $\pi/2$ phase shift. The second pair having twice the azimuthal wavenumber has a $\pi/4$ shift between them with respect to the dominant harmonics. The first pair represents a travelling azimuthal wave with wavenumber $m = 1$, and the second pair indicates a travelling azimuthal wave $m = 2$.
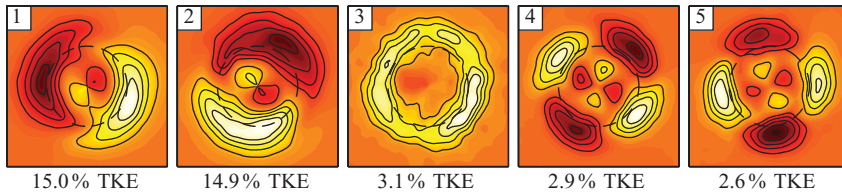
FIGURE 9. First five POD modes of the crossflow plane of measurement; the radial velocity component is shown with contour lines $v_r/\max(v_r) = \{-0.8, -0.6, -0.4, -0.2, 0.2, 0.4, 0.6, 0.8\}$. The POD mode-number p is written in the top-left corner and the percentage of TKE at the bottom. The dashed circle indicates the nozzle diameter.
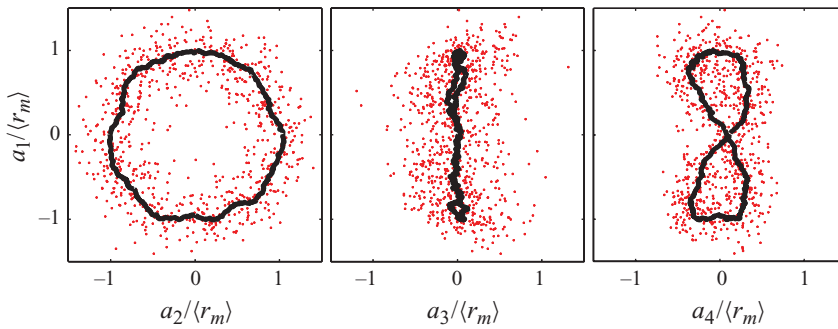

FIGURE 10. Phase portrait of the POD modal amplitudes a_p for the crossflow plane of measurement. The dots represent the experimental data. The solid line is a smoothed fit and similar to Lissajous figures. $A = \overline{\sqrt{a_1^2 + a_2^2}}$ is the mean amplitude of the first two modes (see (4.24)).

To elucidate the temporal behaviour of the identified structures, the phase portraits of the corresponding temporal amplitudes a_p are investigated. Considering the phase portrait of a_1 and a_2 (figure 10), it is clearly seen that the modes describe an oscillating process. In addition, the comparison of a_1 and a_4 reveals that the second mode-pair is the second harmonics with respect to the first one, as indicated by the eight-like form of the Lissajous figure. Both mode pairs describe rotating structures that rotate with the same revolution time with azimuthal wavenumber $m = 1$ for the first and second modes and with $m = 2$ for the fourth and fifth modes. The third mode describes an axisymmetric fluctuation of the flow, which is not correlated with the identified harmonic structures (figure 10). This mode is related to the axial fluctuation of the location of vortex breakdown.

Figure 11 displays the POD modes of the streamwise cross-section. Again, the first two modes have the same azimuthal wavenumber and frequency. These similar modes are axially shifted by a quarter wavelength. They describe coherent structures that are first growing and than decaying in the streamwise direction. The temporal representation of the first two streamwise modes corroborates an oscillating process (figure 12). The first two modes in both crossflow and streamwise planes of measurement describe a harmonically fluctuating structure that the spectral analysis (figure 3) picked up as containing one fundamental frequency. Consequently one may assume that both modes are tied to the same oscillatory structure. Linking the
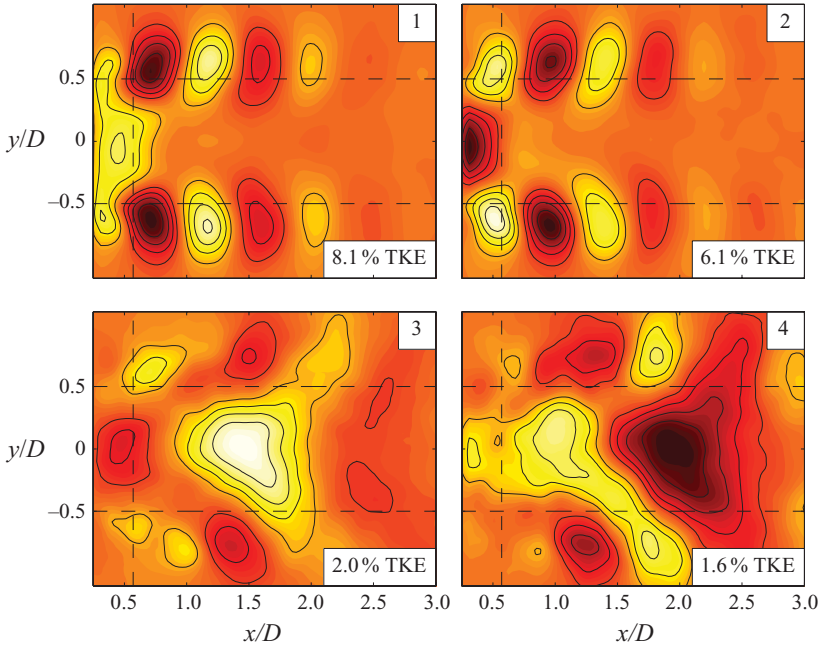
FIGURE 11. First four POD modes of the streamwise measurement plane; the transversal velocity component is shown with contour lines $v_y/\max(v_y) = \{-0.8, -0.6, -0.4, -0.2, 0.2, 0.4, 0.6, 0.8\}$. The mode number is written in the top-right corner and the percentage of TKE in the bottom-right corner. The vertical dashed line indicates the position of the crossflow plane of measurement.
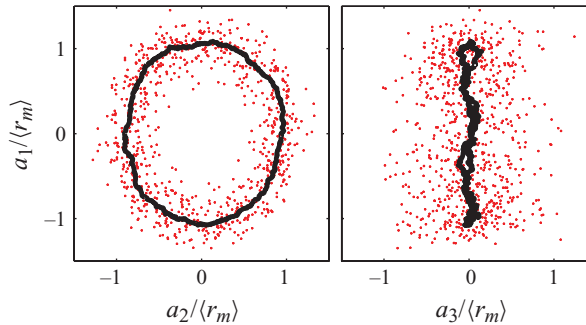

FIGURE 12. Same as figure 10, but with a_p of the streamwise measurement plane.

information from both measurements suggests that the dominant structure is a helical instability mode with azimuthal wavenumber $m = 1$ winding around the recirculation bubble. In this context, the structure at the jet centre (i.e. $r/D = 0$) near the nozzle exit ($x/D < 0.5$), that is visible in the two streamwise modes, is interpreted as being the wavemaker for the global mode.

We note that the relative levels of the first mode-pair with respect to its TKE content are unequal for crosswise and streamwise observation planes. This is due to the dominant structure governing only half of the analysed streamwise measurement domain. Hence, the energy content with respect to the entire streamwise plane is

approximately half as high in comparison to the crosswise plane. Using an appropriate sub-domain for streamwise POD analysis can decrease this difference.

The third and forth streamwise modes (figure 11) are coupled and represent the meandering of the recirculation bubble. The phase portrait reveals no relation to the dominant structure. Hence, the meandering is affected by other processes.

In conclusion, the periodically fluctuating global mode is represented by the first two POD modes in both measurement planes. This harmonic process is indicated by the phase portraits. It is possible to extract the phase information of the dominant coherent structure by identifying the corresponding POD modes. It is then a straightforward procedure to use the temporal amplitudes of these POD modes to obtain the phase angle φ_k for each snapshot k, yielding

$$\widehat{a}_k \, \mathrm{e}^{\mathrm{i}\varphi_k} = a_1(t_k) + \mathrm{i}a_2(t_k). \tag{4.24}$$

This phase angle corresponds to the phase position of a snapshot with respect to the dominant structure, in the manner that the optimal amount of kinetic energy of each snapshot is represented by these modes. Hence, it is possible to define a flow phase via the POD. In the following this definition of phase is used to extract the coherent structures.

4.2.3. *Linking the POD modes to the coherent velocity*

First, we define the coherent velocity $\boldsymbol{v}^c$. Holmes *et al.* (1998) recommend to identify and exploit symmetries in experimental data. This additional filter reduces the complexity of the POD and yields a better understanding of the underlying process. For an axisymmetric swirling jet, the azimuthal direction θ can be regarded as a homogeneous direction, as it is also assumed for linear stability analysis. This direction can be represented through Fourier modes with respect to the azimuthal wavenumber $m = 1$. The triple decomposition assumes the coherent component as being a phase-dependent average of a harmonic signal with temporal period T. Hence, the time can also be regarded as a homogeneous direction and can be decomposed by a Fourier representation according to the phase information φ_k of the POD (4.24). With these simplifications, the coherent velocity reads

$$\boldsymbol{v}^c(x, r, \theta, t) = \mathrm{Re}\{\boldsymbol{F}_{mn}(x, r) \exp[\mathrm{i}(m\theta - n\omega t)]\} \tag{4.25}$$

where m indicates the azimuthal wavenumber, n is a multiple of the fundamental frequency $\omega = 2\pi f$ and $\boldsymbol{F}_{mn}(x, r)$ is a complex-valued vector field containing the radial and axial dependence of the coherent component. The Fourier modes $\boldsymbol{F}_{mn}$ are obtained through a Fourier transform of the fluctuating part of the velocity $\boldsymbol{v}'$:

$$\boldsymbol{F}_{mn}(x, r) = \frac{1}{2\pi T} \int_0^T \int_{-\pi}^{\pi} \boldsymbol{v}'(x, r, \theta, t) \exp[-\mathrm{i}(m\theta - n\omega t)] \, \mathrm{d}\theta \, \mathrm{d}t. \tag{4.26}$$

As described in the previous section, the POD relates each snapshot to a phase angle of the dominant fluctuations. Thus, the Fourier modes $\boldsymbol{F}_{mn}$ are obtained for a discrete time (according to φ_k) and continuous space Fourier transform:

$$\boldsymbol{F}_{mn}(x, r) = \frac{1}{2\pi N} \sum_{k=1}^{N} \int_{-\pi}^{\pi} \boldsymbol{v}'(x, r, \theta, t_k) \exp[-\mathrm{i}(m\theta - n\varphi_k)] \, \mathrm{d}\theta. \tag{4.27}$$

This is valid only if the phase angles φ_k are equally distributed in $[0, 2\pi]$. The phase angles obtained from the POD fulfil this condition, so these angles correspond to a oscillation with uniform frequency $\varphi_k = \omega t_k$.
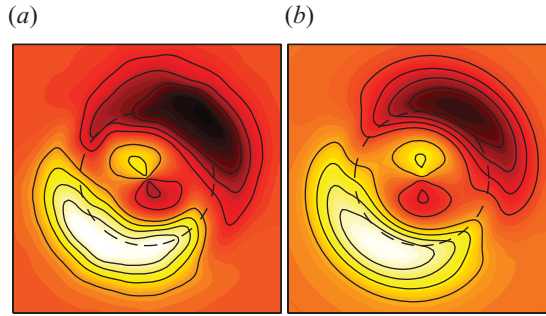
(*a*)   (*b*)

FIGURE 13. Coherent radial velocity v_r^c derived from crossflow measurement via $v^c = \mathrm{Re}\{\boldsymbol{F}_1(r,\theta)\}$ (*a*) is compared with the one derived from streamwise measurement via $v^c = \mathrm{Re}\{\boldsymbol{F}_{11}(r)\,\mathrm{e}^{\mathrm{i}\theta}\}$ (*b*). The flow is visualized by the contour lines $v_r^c/\max(v_r^c) = \{-0.8, -0.6, -0.4, -0.2, 0.2, 0.4, 0.6, 0.8\}$. The dashed circle indicates the nozzle diameter.

The assumed rotational symmetry is examined for the crossflow measurement plane of the vector field. If we omit the assumption of homogeneity in θ of (4.25), then the complex coherent component is given by

$$\boldsymbol{F}_n(x, r, \theta) = \frac{1}{N} \sum_{k=1}^{N} \boldsymbol{v}'(x, r, \theta, t_k)\, \mathrm{e}^{\mathrm{i}n\varphi_k}. \tag{4.28}$$

This equals the definition of POD modes (4.21) provided the first two POD modes are considered in a complex representation with $\widehat{a}_k\,\mathrm{e}^{\mathrm{i}\varphi_k} = a_1(t_k) + \mathrm{i}a_2(t_k)$, except that the amplitude $\widehat{a}_k$ of the temporal modes is neglected. We assume the amplitude variations to be caused by turbulent noise, which is indicated by the phase portrait in figure 13 (see also Depardon *et al.* 2007). In consequence, the spatial POD modes are similar to the coherent component, in detail $\boldsymbol{\Phi}_1 + \mathrm{i}\boldsymbol{\Phi}_2 \approx \boldsymbol{F}_1$ (with $\boldsymbol{F}_n$ as in (4.28)).

In figure 13, the coherent component $\boldsymbol{v}^c$ in the crosswise measurement plane is compared between the simple phase-average derived from crosswise data $\boldsymbol{v}^c = Re\{\boldsymbol{F}_1(r,\theta)\}$ and the phase-average constructed from streamwise data assuming azimuthal symmetry $\boldsymbol{v}^c = \mathrm{Re}\{\boldsymbol{F}_{11}(r)\,\mathrm{e}^{\mathrm{i}\theta}\}$. The contour plots of $\boldsymbol{v}^c$ are very similar proving that the assumed symmetry is legitimate. The discrepancy between the two plots is attributed to an insufficient number of snapshots for more precise averaging.

It should be noted that the triple decomposition, as outlined in this section, is not limited to the use of POD. The phase information of oscillatory fluctuations is often inferred in three different ways. First, if the flow is externally actuated, the phase information can be directly derived from the actuation signal. Second, it is possible to obtain the required phase information from a time-resolved point measurement (e.g. hot wire), using a bandpass filter and a Hilbert transformation. Third, it is provided by a statistical approach such as the POD described above. In the present investigation, the POD was chosen because it has some advantages with respect to the other techniques which will be shortly depicted.

Most flow oscillations do not occur at a prescribed frequency, as there is always jitter. Filtering with respect to a fixed frequency will ignore large portions of the flow affected by frequency modulation, reappearing in $\boldsymbol{v}^s$. With a locally adjusted frequency, we reduce the amount of TKE captured by $\boldsymbol{v}^s$, while $\boldsymbol{v}^c$ lumps a narrow frequency band into a single frequency. In the case of a phase average, triggered by external forcing, no phase jitter is incorporated at all. If a time-resolved sensor is used, the amount of phase jitter accounted for depends on the bandwidth of the

bandpass filter used. When using the POD phase, obtained according to (4.24), no fixed frequency has to be assumed, and the calculated phase is the optimal one in terms of energy representation. The optimal phase is related to the optimality of spatial POD modes, where these modes are understood as a prior guess for coherent structures providing the phase through projection on the snapshots. Furthermore, in contrast to a time-resolved point measurement, the POD approach predicts the phase angle from spatial modes and not from one single point in the flow yielding a more accurate prediction of the global phase.

4.2.4. *Construction of three-dimensional coherent structures*

It is now straightforward to construct 3D-velocity data from the two measurement planes utilizing the identified symmetries of the coherent velocity v^c discussed in the previous section. The approach for this construction is graphically outlined in figure 14, illustrating the main steps in this section.

(*a*) Identification of a fundamental frequency by time-resolved point measurement.

(*b*) POD analysis of the PIV data in the two measurement planes, which identifies dominant structures and provides the related phase information.

(*c*) Calculation of coherent structures with phase information and identification of azimuthal symmetries through a Fourier transform.

(*d*) Construction of 3D data of the coherent structure using the identified symmetries to extrapolate data from 2D measurement plane.

In the final step, the streamwise measurement plane (r–x-plane) gives the axial and radial dependence of the coherent complex amplitude $F_{mn}(x, r)$ (4.26). As shown in the previous section, the fundamental frequency is related to the azimuthal wavenumber $m = 1$ and first harmonic $n = 1$. Combining this information in (4.25), a spatio-temporal representation of the coherent velocity is given by

$$v^c(x, r, \theta, t) = \text{Re}\{F_{11}(x, r) \exp[i(\theta - \omega t)]\}. \tag{4.29}$$

5. Results

5.1. *Most unstable spatial modes*

Before we discuss the results obtained from the linear stability analysis, we would like to recall its simplifying assumptions. Due to the occurrence of vortex breakdown, the underlying time-averaged flow exhibits strong gradients in the axial direction. Hence, the employed parallel-flow assumption for the normal mode decomposition (4.4) is violated due to these gradients. Various approaches have been developed to overcome this shortcoming of the linear theory, generally restricted to small deviations. Intriguingly, wavelength and radial amplitude distribution are often found to be reasonably well approximated by the eigensolution of the Orr–Sommerfeld equation solely based on a locally parallel flow. In this study, we do not pause to incorporate non-parallel effects.

In the scheme of linear stability analysis, the spatial amplification rate α_i is computed for the azimuthal wavenumber $m = 1$ in order to derive the coherent velocity of the single helical instability mode that is observed in the experiment. The complex wavenumber was calculated for real frequencies in the range $0 \leqslant \omega \leqslant 6$ at four different axial locations. The spatial branches are displayed in figure 15. Note that the frequency ω is normalized by the length scale $R(x)$ and velocity scale $V(x)$ (see §4.1.1), whereas the Strouhal number St associated with the global oscillation frequency is based on the bulk velocity U and nozzle diameter D. The global frequency expressed
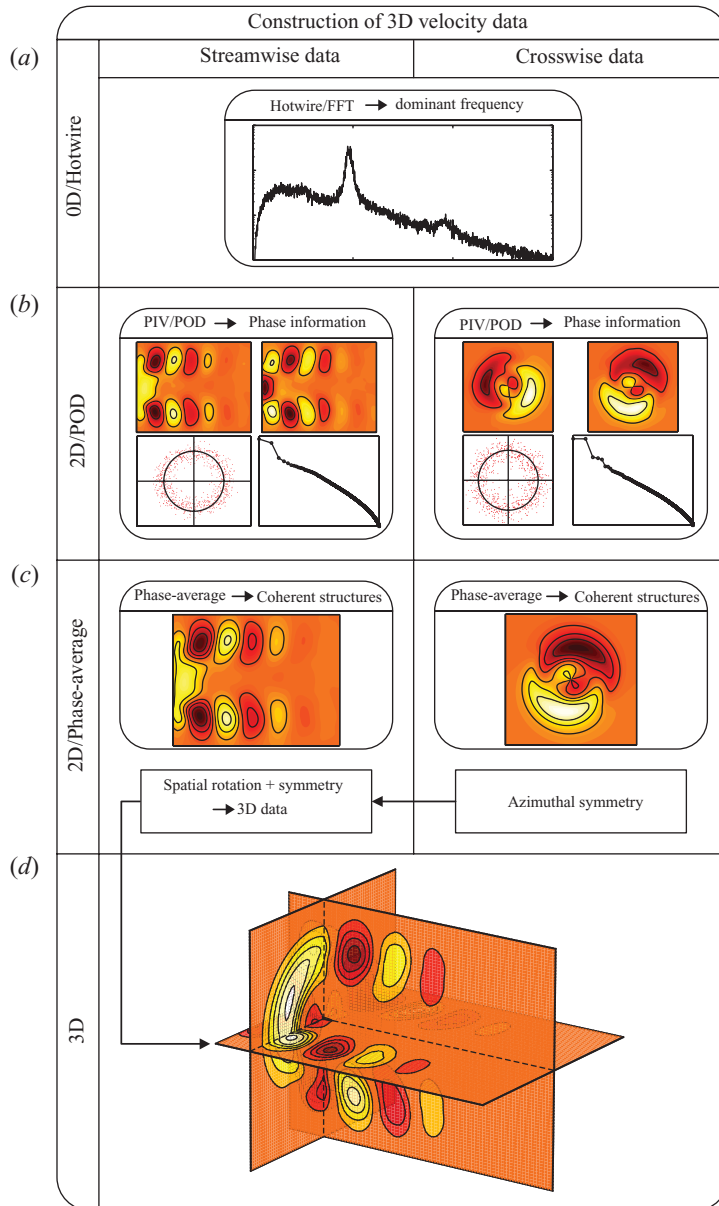
FIGURE 14. Schematic diagram of the 3D flow construction. The illustrated steps are as follows: (*a*) identification of the fundamental frequency; (*b*) POD analysis of the PIV data yielding the flow phase; (*c*) identification of coherent structures and symmetries and (*d*) construction of 3D data from the 2D measurements.

by ω increases in the downstream direction as the downstream increase of R is more rapid than the decay of U (see the open circles in figure 15). At the axial locations where the flow is unstable to the global frequency, only one unstable spatial branch is found and the spatial amplification rate can easily be tracked in the downstream direction. Waves forced at the global frequency grow rapidly near the nozzle exit where the shear layer is thin relative to the nozzle radius. As the shear layer spreads
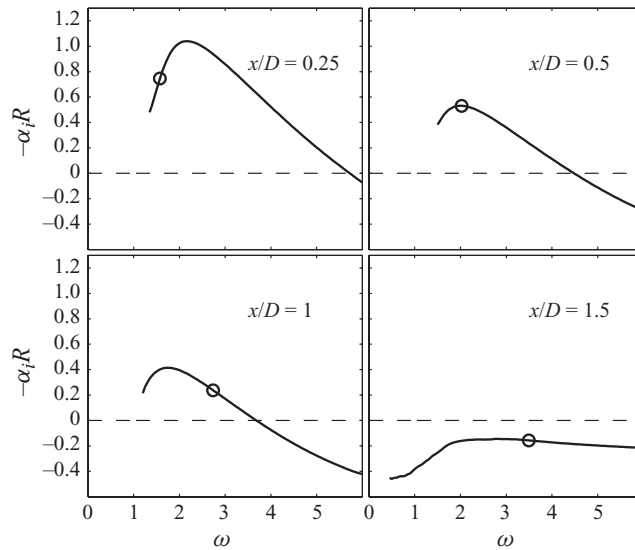
FIGURE 15. Spatial amplification rate of the mode $m = 1$ versus dimensionless real frequency ω at different cross-sections. The open circle marks the measured frequency of the mode $m = 1$ indicating the growth ($x/D \leqslant 1$) and decay ($x/D = 1.5$) of the most unstable mode.
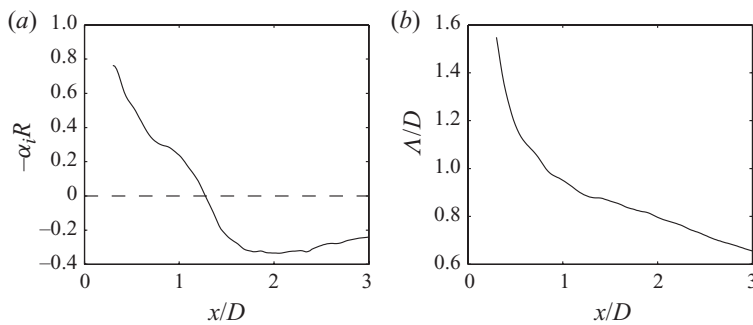

FIGURE 16. Streamwise evolution of the spatial amplification rate (a) and axial wavelength $\Lambda = 2\pi R/\alpha_r$ (b) of the most unstable mode $m = 1$ based on local analysis.

in the radial direction with increasing downstream distance, the spatial amplification rate at $St = 0.49$ decreases. The corresponding spatial branch downstream of the point of neutral amplification is stable for all frequencies.

The evolution of the spatial growth rate α_i with downstream distance is investigated in detail by computing the eigenmodes for various streamwise locations at the global frequency of $St = 0.49$ (figure 16). Accordingly, the spatial growth rate decreases continuously with downstream distance reaching natural amplification at $x/D = 1.28$. Downstream of the neutral point, the decaying rate increases in the axial direction up to $x/D = 2$. In the decaying region several modes coexist and the spatial branch that corresponds to the most unstable mode is tracked from the unstable regime where only one mode exists by minimizing the distance between the eigenfunctions and eigenvalues (see the last paragraph of section 4.1.3 for further details). Note that in the bottom-right frame of figure 15, only the spatial branch that corresponds to the most unstable mode is shown. The computed axial wavelength of the
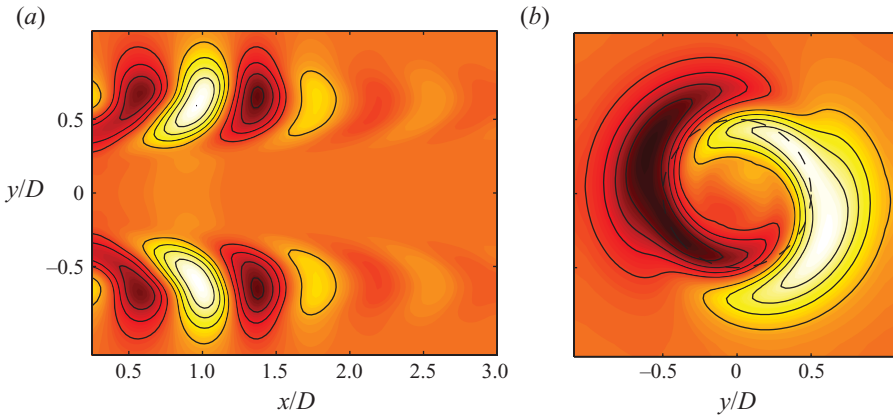
FIGURE 17. Coherent velocity of the most amplified normal mode. Eigenfunctions are shown at an arbitrary phase-angle. The contour lines represent $v_r^c / \max(v_r^c) = \{-0.8, -0.6, -0.4, -0.2, 0.2, 0.6, 0.4, 0.8\}$. The eigenvalue problem (4.9) was solved for the azimuthal wavenumber $m = 1$ and global frequency $St = 0.49$. The dashed circle in (b) indicates the nozzle diameter which approximately separates the inner and the outer shear layer. (a) Transversal coherent velocity v_y^c. (b) Radial coherent velocity v_r^c at $x/D = 0.57$.

most amplified mode is displayed as a function of x/D in figure 16. The rapid decrease in wavelength in the axial direction is caused by non-parallel effects. The convectively unstable modes are amplified at constant frequency while they travel downstream. Due to the pronounced jet widening, their convection velocity, that is related to U, is rapidly decaying in the axial direction, thus causing the wavelength to decrease.

The accuracy of the stability analysis is validated by comparing the computed eigenfunctions with the actually measured phase-averaged velocities described in §4. The eigenfunction of the most amplified mode is computed at $x/D = 0.57$, the axial location where crossflow measurements were conducted. Comparing the empirical mode, displayed in figure 13, to the stability mode, displayed in figure 17(b), shows obvious similarities. Both modes agree well in the outer region of the jet where they are most energetic ($|y/D| > 0.5$). In the inner region the structures seem to be out of phase and the coherent velocity near the jet core that is evident from the measurements is not modelled by the eigenmodes. As stated previously, the present stability analysis is only valid for the outer convective unstable region of the jet. In particular, near the jet core close to the nozzle exit where coherent velocity indicates the location of the wavemaker, the present analysis should produce wrong estimations. Further downstream of the wavemaker, the agreement of the eigenmodes to the phase-averaged measurements improves even for the inner region of the jet. This is shown by constructing the streamwise shape of the global mode from the locally computed eigenfunctions and eigenvalues. According to Gaster (1968), the overall growth of a disturbance can be calculated by integrating the complex α along x, yielding

$$[v_x^c, v_r^c, v_\theta^c, p^c] = \mathrm{Re}\left\{[H, iF, G, P]\exp\left[i\left(\int_{x_0}^x \alpha\,\mathrm{d}x + m\theta - \omega t\right)\right]\right\}, \qquad (5.1)$$

where α is complex and x_0 is the location of the first measured profile with $x_0/D = 0.2$. In order to consistently ensemble the local eigenmodes to a global solution, the eigenvector X was normalized using the Euclidean norm $\|X\| = \sqrt{(X, X)}$, and the
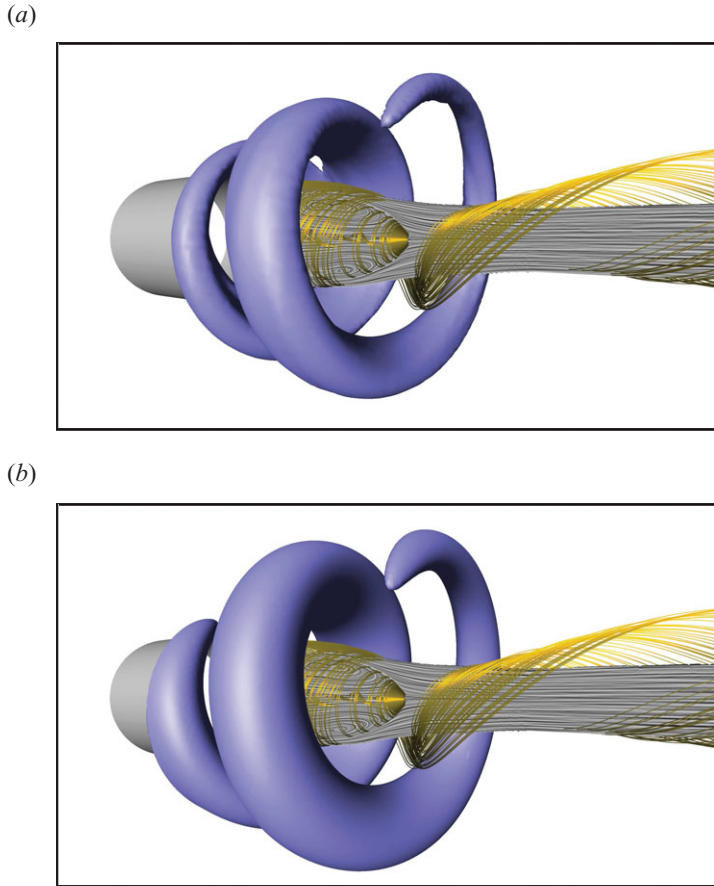
(*a*)

(*b*)

FIGURE 18. Three-dimensional flow field visualizing the global mode $m = 1$ that is dominating the near field of a strongly swirled jet ($Re_D = 20\,000$; $S = 1.22$). The blue iso-contour represents the constant azimuthal vorticity of phase-averaged velocities indicating the streamwise growth of a single helical instability in the outer region of the jet. Streamlines and LIC surface are based on the time-averaged flow, visualizing the recirculation bubble and the sense of rotation of the swirling jet. (*a*) Empirically extracted coherent structure using POD. (*b*) Theoretically extracted coherent structure using linear stability analysis.

phase angle was equalized at the characteristic jet radius R. The resulting coherent velocity distribution along the streamwise plane is shown in figure 17(*a*).

Except for the jet core region upstream $x/D = 0.7$ where the wavemaker is located, the computations agree well with the empirical POD modes shown in figure 11. The axial wavelength and the radial amplitude distribution are well estimated. Even the overall amplification is well approximated with the maximum coherent amplitude at $x/D \approx 1.25$ and the decaying region further downstream.

5.2. *Three-dimensional shape of the global mode*

Finally, the empirically extracted mode and the mode derived from the stability model are constructed in the entire three-dimensional domain. By adding the time-averaged mean flow to the coherent velocities, the global mode renders a physically plausible shape as can be seen in figure 18. The blue helix represents an iso-surface having constant phase-averaged azimuthal vorticity. For the upper figure the phase average

was derived applying the empirical approach based on the POD as outlined in § 4.2, whereas for the lower figure the phase-averaged velocity was derived from the linear stability analysis based on the analytically approximated mean flow as outlined in § 4.1. Both methods reveal the same structure. It represents the $m = 1$ mode that rotates in the clockwise direction with the base flow at a rotation rate corresponding to $St = 0.49$. The yellow streamlines and the grey LIC-surface (linear integral convolution; see e.g. Cabral & Leedom 1993; Stalling & Hege 1995) are computed from the actually measured time-averaged flow. The streamlines are intended to visualize the direction of rotation of the mean flow and also indicate the mean boundary of the recirculation bubble. Note that the streamlines are orientated perpendicularly to the roll-axis of the helical mode. Accordingly, the helical structure is co-rotating but counter-winding. Similar observations have been found in experiments by Liang & Maxworthy (2005) and in DNS computations conducted by Ruith et al. (2003). The LIC surface visualizes the flow structures inside the recirculation bubble showing a stationary ring-like vortex. This structure must be carefully interpreted because the time-averaged flow field of the inner region of the recirculation bubble differs strongly from the phase-averaged or instantaneous flow. It is observed that the entire recirculation bubble meanders around the jet centre in phase with the outer coherent structure. As mentioned above, the frequency of the global mode is dictated by the wavemaker located on the jet centre. This precessing of the vortex core is not visible in figure 18 since the level of the vorticity iso-contour was selected to most properly visualize the structures in the outer region of the jet and is therefore too high for visualizing the structures located in the interior of the jet.

6. Concluding remarks

The coherent structures of strongly swirled jets undergoing vortex breakdown were investigated. The nature of these structures was phenomenologically observed, whereupon power spectra measured by a hot wire indicated that this flow regime exhibits pronounced harmonic oscillations. The origin of these oscillations was studied by two independent experimental techniques. First, the lock-in behaviour of the forced flow was investigated and it revealed a linear relationship between the forcing frequency and the critical lock-in amplitude. Second, the limit-cycle amplitude of the dominant mode was observed to be proportional to the square root of the deviation from the swirl magnitude considered as a control parameter. Both observations corroborate quantitative relationships of a self-excited oscillatory global mode originating from a supercritical Hopf bifurcation. In other words, the results are consistent with mean-field theory. The phase-averaged velocities show the existence of a co-rotating counter-winding helical mode. Most energy of its intensity is located in the outer region of the jet. A similar structure was observed experimentally by Liang & Maxworthy (2005) and in numerical simulations by Ruith et al. (2003). Theoretical considerations of Gallaire et al. (2006) suggest that the self-excited global mode originates from a local region of absolute instability located in the jet centre. These results are confirmed by our observation where a strong precessing of the vortex core sets the pace of the amplified instabilities in the outer part of the jet.

The observed oscillatory helical structures were then closely examined. Starting with an experiment using 2D uncorrelated PIV snapshots in a streamwise and a crossflow plane, the 3D time-dependent coherent structures were extracted by kinematic and dynamic considerations, exploiting the observed dominant periodicity

of the flow. The kinematic velocity field reconstruction started from the uncorrelated 2D streamwise velocity fields determined by PIV. The pronounced oscillatory nature of the fluctuations was evidenced by two leading POD modes spanning a corresponding convecting vortex pattern. These two POD modes allowed one to attribute a phase to each snapshot taken. A continuous time dependence was imposed by assuming a single oscillation frequency, consistent with the experimental measurements. This assumption allows for restoration of time dependence provided that small-amplitude variations of the turbulent flow such as the less-energetic higher harmonics and stochastic small-scale fluctuations are negligible. A 3D flow pattern was reconstructed by exploiting an azimuthal symmetry of the observed helical coherent structures. The resulting 3D flow pattern corroborates PIV observations in crossflow planes. Thus, the spatio-temporal evolution of the full 3D helical structure was obtained from 2D uncorrelated data sets.

The velocity field of the global mode was also derived by means of a linear stability analysis employing the measured mean flow. A spatial approach was justified by previous experiments conducted by the authors, showing that the wavemaker generating the global oscillations is located inside the jet central core upstream of the recirculation bubble imposing its frequency on the outer shear layer where instabilities are convective. Hence, for a purely spatial analysis, the precessing vortex core upstream of the vortex breakdown location was considered as a 'natural oscillator' and the convectively unstable surrounding flow field was modelled as being externally forced. The spatial approach is corroborated *a posteriori* by the good agreement of the stability eigenmodes, amplification rates and wavelengths with the corresponding quantities of the measured phase-averaged flow, particularly in the periphery of the recirculation bubble. The theoretical prediction was less accurate in the interior of the jet near the wavemaker location due to the convective type of the analysis. The good agreement in the convective unstable region also gives credibility to the above-mentioned empirical reconstruction of the 3D time-periodic flow, using the same velocity field ansatz.

Finally, a three-dimensional portrait of the global mode was constructed from experimental data and from the theoretical model. Both approaches represent a co-rotating, counter-winding single helical coherent structure that is wrapped around the recirculation zone – in a remarkable agreement. The vortex axis is perpendicular to the mean flow direction which is characteristic for the Kelvin–Helmholtz type of instability. The good agreement between instability and POD-based eigenmodes is neither self-evident nor completely unusual in free shear flows. Our study reveals that the highly swirled jet has similar dynamics as, e.g. the wake flow with an absolutely unstable clock-work of vortex shedding in the recirculation zone and convectively moving structures in the far wake. Moreover, our study provides simple and effective kinematic and dynamic tools that complete the coherent-structure extraction from 2D PIV data. The proposed approach is expected to be applicable to a large class of other shear flows.

They also wish to thank the reviewers for their helpful suggestions for improvement of an earlier draft.

REFERENCES

Billant, P., Chomaz, J.-M. & Huerre, P. 1998 Experimental study of vortex breakdown in swirling jets. *J. Fluid Mech.* **376**, 183–219.

Cabral, B. & Leedom, L. C. 1993 Imaging vector fields using line integral convolution. In *Proceedings of the 20th Annual Conference on Computer Graphics and Interactive Techniques (SIGGRAPH)*, Anaheim, CA, pp. 263–270.

Cantwell, B. J. 1981 Organized motion in turbulent flow. *Annu. Rev. Fluid Mech.* **13**, 457–515.

Chigier, N. & Chervinsky, A. 1965 Experimental and theoretical study of turbulent swirling jets issuing from a round orifice. *Isr. J. Technol.* **4**, 44–54.

Chomaz, J.-M. 2005 Global instabilities in spatially developing flows: non-normality and nonlinearity. *Annu. Rev. Fluid Mech.* **37**, 357–392.

Cohen, J., Marasli, B. & Levinski, V. 1994 Interaction between the mean flow and coherent structures in turbulent mixing layers. *J. Fluid Mech.* **260**, 81–94.

Cohen, J. & Wygnanski, I. 1987 The evolution of instabilities in the axisymmetric jet. Part I. The linear growth of disturbances near the nozzle. Part II. The flow resulting from the interaction between two waves. *J. Fluid Mech.* **176**, 191–219.

Crighton, D. G. & Gaster, M. 1976 Stability of slowly diverging jet flow. *J. Fluid Mech.* **77**, 397–413.

Depardon, S., Lasserre, J. J., Brizzi, L. E. & Borée, J. 2007 Automated topology classification method for instantaneous velocity fields. *Exp. Fluids* **42**, 697–710.

Duwig, C. & Fuchs, L. 2007 Large eddy simulation of vortex breakdown/flame interaction. *Phys. Fluids* **19**, 5103.

Escudier, M. P. & Keller, J. J. 1985 Recirculation in swirling flow. A manifestation of vortex breakdown. *AIAA J.* **23**, 111–116.

Faler, J. H. & Leibovich, S. 1978 An experimental map of the internal structure of a vortex breakdown. *J. Fluid Mech.* **86**, 313–335.

Freymuth, P. 1966 On transition in a separated laminar boundary layer. *J. Fluid Mech.* **25**, 683–704.

Gallaire, F. & Chomaz, J.-M. 2003 Mode selection in swirling jet experiments: a linear stability analysis. *J. Fluid Mech.* **494**, 223–253.

Gallaire, F., Chomaz, J.-M. & Huerre, P. 2004 Closed-loop control of vortex breakdown: a model study. *J. Fluid Mech.* **511**, 67–93.

Gallaire, F., Rott, S. & Chomaz, J.-M. 2004 Experimental study of a free and forced swirling jet. *Phys. Fluids* **16**, 2907–2917.

Gallaire, F., Ruith, M., Meiburg, E., Chomaz, J.-M. & Huerre, P. 2006 Spiral vortex breakdown as a global mode. *J. Fluid Mech.* **549**, 71–80.

Gaster, M. 1968 Growth of disturbances in both space and time. *Phys. Fluids* **11**, 723–727.

Gaster, M. 1974 On the effects of boundary-layer growth on flow stability. *J. Fluid Mech.* **66**, 465–480.

Gaster, M., Kit, E. & Wygnanski, I. 1985 Large-scale structures in a forced turbulent mixing layer. *J. Fluid Mech.* **150**, 23–39.

Ho, C.-M. & Huerre, P. 1984 Perturbed free shear layers. *Annu. Rev. Fluid Mech.* **16**, 365–424.

Holmes, P., Lumley, J. L. & Berkooz, G. 1998 *Turbulence, Coherent Structures, Dynamical Systems and Symmetry*. Cambridge University Press.

Huerre, P. & Monkewitz, P. A. 1990 Local and global instabilities in spatially developing flows. *Annu. Rev. Fluid Mech.* **22**, 473–537.

Hussain, A. K. M. F. & Reynolds, W. C. 1970 The mechanics of an organized wave in turbulent shear flow. *J. Fluid Mech.* **41**, 241–258.

Juniper, M. P., Li, L. K. & Nichols, J. W. 2009 Forcing of self-excited round jet diffusion flames. *Proc. Combust. Inst.* **32** (1), 1191–1198.

Khorrami, M. R. 1991 On the viscous modes of instability of a trailing line vortex. *J. Fluid Mech.* **225**, 197–212.

KHORRAMI, M. R., MALIK, M. R. & ASH, R. L. 1989 Application of spectral collocation techniques to the stability of swirling flows. *J. Comput. Phys.* **81** (1), 206–229.

LAMBOURNE, N. C. & BRYER, D. W. 1962 The bursting of leading-edge vortices: some observations and discussion of the phenomenon, *Tech. Rep.* Ministry of Aviation, Aeronautical Research Council, vol. 3282.

LANDAU, L. D. & LIFSHITZ, E. M. 1959 *Fluid Mechanics*. Pergamon.

LAUFER, J. 1975 New trends in experimental turbulence research. *Annu. Rev. Fluid Mech.* **7**, 307–326.

LIANG, H. & MAXWORTHY, T. 2005 An experimental investigation of swirling jets. *J. Fluid Mech.* **525**, 115–159.

LIU, J. 1989 Coherent structures in transitional and turbulent free shear flows. *Annu. Rev. Fluid Mech.* **21**, 285–315.

LUDWIEG, H. 1961 Ergänzung zu der Arbeit: Stabilität der Strömung in einem zylindrischen Ringraum. *Z. Flugwiss.* **9**, 359.

LUMLEY, J. L. 1967 *Atmospheric Turbulence and Radio Wave Propagation*. Elsevier.

MALIK, M. R., ZANG, T. A. & HUSSAINI, M. Y. 1985 A spectral collocation method for the Navier–Stokes equations. *J. Comput. Phys.* **61**, 64–88.

MARTINELLI, F., OLIVANI, A. & COGHE, A. 2007 Experimental analysis of the precessing vortex core in a free swirling jet. *Exp. Fluids* **42**, 841–841.

MICHALKE, A. 1965 On spatially growing disturbances in an inviscid shear layer. *J. Fluid Mech.* **23**, 521–544.

MICHALKE, A. 1999 Absolute inviscid instability of a ring jet with back-flow and swirl. *Eur. J. Mech.* **18**, 3–12.

MONKEWITZ, P. A., HUERRE, P. & CHOMAZ, J.-M. 1993 Global linear stability analysis of weakly non-parallel shear flows. *J. Fluid Mech.* **251**, 1–20.

MONKEWITZ, P. A. & SOHN, K. D. 1988 Absolute instability in hot jets. *AIAA J.* **26**, 911–916.

NOACK, B. R., AFANASIEV, K., MORZYŃSKI, M., TADMOR, G. & THIELE, F. 2003 A hierarchy of low-dimensional models for the transient and post-transient cylinder wake. *J. Fluid Mech.* **497**, 335–363.

OBERLEITHNER, K., LÜCK, M., PASCHEREIT, C. O. & WYGNANSKI, I. 2009 Control of vortex breakdown in critical swirl regime using azimuthal forcing. In *Minnowbrook VI, Syracuse University*.

OLENDRARU, C. & SELLIER, A. 2002 Viscous effects in the absolute convective instability of the Batchelor vortex. *J. Fluid Mech.* **459**, 371–396.

PANDA, J. & MCLAUGHLIN, D. K. 1994 Experiments on the instabilities of a swirling jet. *Phys. Fluids* **6**, 263–276.

PARRAS, L. & FERNANDEZ-FERIA, R. 2007 Spatial stability and the onset of absolute instability of Batchelor's vortex for high swirl numbers. *J. Fluid Mech.* **583**, 27.

PIER, B. & HUERRE, P. 2001 Nonlinear self-sustained structures and fronts in spatially developing wake flows. *J. Fluid Mech.* **435**, 145–174.

PLASCHKO, P. 1979 Helical instabilities of slowly divergent jets. *J. Fluid Mech.* **92**, 209–215.

PROVANSAL, M., MATHIS, C. & BOYER, L. 1987 Benard-von Karman instability: transient and forced regimes. *J. Fluid Mech.* **182**, 1–22.

RAJARATNAM, N. 1976 *Turbulent Jets (Developments in Water Science, vol 5)*. Elsevier.

ROSHKO, A. 1977 Errata: structure of turbulent shear flows: a new look. *AIAA J.* **15**, 768–768.

ROWLEY, C. 2005 Model reduction for fluids using balanced proper orthogonal decomposition. *Intl J. Bifurcation Chaos* **15** (3), 997–1013.

ROWLEY, C. W., MEZIĆ, I., BAGHERI, S., SCHLATTER, P. & HENNINGSON, D. S. 2009 Spectral analysis of nonlinear flows. *J. Fluid Mech.* **641**, 115.

RUITH, M. R., CHEN, P., MEIBURG, E. & MAXWORTHY, T. 2003 Three-dimensional vortex breakdown in swirling jets and wakes: direct numerical simulation. *J. Fluid Mech.* **486**, 331–378.

SARPKAYA, T. 1971 On stationary and travelling vortex breakdowns. *J. Fluid Mech.* **45**, 545–559.

SCHMID, P. J. 2010 Dynamic mode decomposition of numerical and experimental data. *J. Fluid Mech.* **656**, 5–28.

SIROVICH, L. 1987 Turbulence and the dynamics of coherent structures. Part I. Coherent structures. *Q. Appl. Math.* **XLV**, 561–571.

SREENIVASAN, K. R., RAGHU, S. & KYLE, D. 1989 Absolute instability in variable density round jets. *Exp. Fluids* **7**, 309–317.

STALLING, D. & HEGE, H.-C. 1995 Fast and resolution independent line integral convolution. In *Proceedings of the 22nd annual conference on Computer graphics and interactive techniques (SIGGRAPH),* Los Angeles, CA, pp. 249–256.

STUART, J. 1958 On the non-linear mechanics of hydrodynamic stability. *J. Fluid Mech.* **4**, 1–21.

TOWNSEND, A. 1956 *The Structure of Turbulent Shear Flow.* Cambridge University Press.

VAN DYKE, M. 1975 *Perturbation Methods in Fluid Mechanics*, annotated edn. The Parabolic Press.

WEISBROT, I. & WYGNANSKI, I. 1988 On coherent structures in a highly excited mixing layer. *J. Fluid Mech.* **195**, 137.